sensors

MDPI

Article

Active Alignment of Large-Aperture Space Telescopes for Optimal Ellipticity Performance

Xiaoquan Bai [1,2], Xixi Gu [1,2], Boqian Xu [1,2], Fengyi Jiang [1,2], Zhirong Lu [1,2], Shuyan Xu [1,2] and Guohao Ju [1,2,*]

[1] Changchun Institute of Optics, Fine Mechanics and Physics, Chinese Academy of Sciences, Changchun 130033, China; baixiaoquan@ciomp.ac.cn (X.B.); guxixi@ciomp.ac.cn (X.G.); ciomp_xubq@126.com (B.X.); jiangfengyi@ciomp.ac.cn (F.J.); luzhirong18@mails.ucas.edu.cn (Z.L.); xusy@ciomp.ac.cn (S.X.)

[2] Chinese Academy of Sciences Key Laboratory of On-Orbit Manufacturing and Integration for Space Optics System, Changchun 130033, China

* Correspondence: juguohao@ciomp.ac.cn

Abstract: Ellipticity performance of space telescopes is important for exploration of dark matter. However, traditional on-orbit active optical alignment of space telescopes often takes "minimum wavefront error across the field of view" as the correction goal, and the ellipticity performance after correcting the wave aberration is not optimal. This paper proposes an active optical alignment strategy to achieve optimal ellipticity performance. Based on the framework of nodal aberration theory (NAT), the aberration field distribution corresponding to the optimal full field-of-view ellipticity is determined using global optimization. The degrees of freedom (DOFs) of the secondary mirror and the folded flat mirror are taken as the compensation DOFs to achieve the optimal ellipticity performance. Some valuable insights into aberration field characteristics corresponding to optimal ellipticity performance are presented. This work lays a basis for the correction of ellipticity for complicated optical systems.

Keywords: active optical alignment; ellipticity performance; space telescope

Citation: Bai, X.; Gu, X.; Xu, B.; Jiang, F.; Lu, Z.; Xu, S.; Ju, G. Active Alignment of Large-Aperture Space Telescopes for Optimal Ellipticity Performance. *Sensors* **2023**, *23*, 4705. https://doi.org/10.3390/s23104705

Academic Editor: Xin Zhu

Received: 17 April 2023
Revised: 5 May 2023
Accepted: 10 May 2023
Published: 12 May 2023

1. Introduction

Point-spread function (PSF) ellipticity of space telescopes is of great significance for the exploration of dark matter and dark energy. Dark matter and dark energy do not absorb, emit or radiate light, so they cannot be observed directly, and can only be observed indirectly by using the weak gravitational lensing effect. At present, the strength of the weak gravitational lensing effect is mainly measured by the change in the ellipticity of stars or galaxies. Therefore, accurate measurement of the ellipticity of stars or galaxies in the universe is of great significance for the observation and research of dark matter and dark energy.

Influence of weak gravitational lens effect on the ellipticity of celestial bodies or galaxies is very weak [1–3]. In order to accurately measure it, the change in ellipticity caused by the optical system itself should be limited to a very small range so as to minimize the influence of the ellipticity of the optical system on the observation of dark matter and dark energy. The ellipticity of the optical system itself is mainly caused by the asymmetrical pupil shape and wave aberration of the optical system itself [4]. Generally speaking, the smaller the wave aberration is, the smaller the ellipticity of the point-spread function is. However, the "full field wave aberration optimization" and "full field point-spread function ellipticity optimization" of optical system essentially correspond to two different system states and cannot be confused.

It is critical to align large aperture space telescope on orbit [5,6]. At present, active alignment methods are mainly divided into two classes: numerical method and analytic

method. On the numerical computing side, sensitive table method (STM) [7], artificial neural networks method (ANN) [8], merit function (MF) regression method [9–11], differential wavefront sampling (DWS) [12–14] and image features [15–17] are widely used in ground alignment. The analytical method is mainly nodal aberration theory (NAT) [18–23]. Importantly, NAT provides an aberration model that yields to obtain insight into the aberration response to misalignments [24–27] and guide optical alignment [28–37].

However, traditional on-orbit active optical alignment of space telescopes often takes "optimal wavefront aberration in the full field of view" as the correction goal, and the ellipticity performance after correcting the wave aberration is not optimal. It is necessary to formulate different correction targets for different astronomical observation needs of space telescopes. Specifically, when observing dark matter and dark energy, the mode of "optimal ellipticity performance in the full field of view" is adopted to make the point-spread function ellipticity caused by the optical system itself as small as possible so as to better identify and judge the weak gravitational lens effect caused by dark matter and dark energy.

In this paper, an active alignment strategy to achieve optimal ellipticity performance is proposed. Chinese Space Station Telescope (CSST) is taken as an example to demonstrate its performance. (At the beginning of CSST design, the distribution of ellipticity and wavefront aberration was balanced. Correcting ellipticity is one of the requirements for CSST in orbit. The results of integrated simulation analysis (for CSST) are used for simulation analysis in this paper.). Based on the framework of nodal aberration theory (NAT), the aberration field distribution corresponding to the optimal full field-of-view ellipticity is determined using global optimization. In this process, the objective function is the mean ellipticity value of 41*41 field points and all misalignments of mirrors are taken as the variable. Then, the degrees of freedom (DOFs) of the secondary mirror and the folded flat mirror are taken as the compensation DOFs to achieve the optimal ellipticity performance on orbit. Some valuable insights into aberration field characteristics corresponding to the optimal ellipticity performance are also presented concerning the proportion of different aberration types.

2. Ellipticity

The ellipticity of PSF under certain perturbations is defined as follows [38–43]:

$$e\left(\vec{H},\mathbf{v}\right)=\sqrt{\left[e_1\left(\vec{H},\mathbf{v}\right)\right]^2+\left[e_2\left(\vec{H},\mathbf{v}\right)\right]^2}, \tag{1}$$

where $\mathbf{v}$ includes misalignment parameters of the optical system, $\vec{H}$ represents field position of the PSF, and e_1 and e_2 are the two components of the PSF ellipticity, which can be expressed as

$$\begin{cases} e_1\left(\vec{H},v\right)=\dfrac{Q_{XX}\left(\vec{H},\mathbf{v}\right)-Q_{YY}\left(\vec{H},\mathbf{v}\right)}{Q_{XX}\left(\vec{H},\mathbf{v}\right)+Q_{YY}\left(\vec{H},\mathbf{v}\right)} \\ e_2\left(\vec{H},v\right)=\dfrac{2Q_{XY}\left(\vec{H},v\right)}{Q_{XX}\left(\vec{H},\mathbf{v}\right)+Q_{YY}\left(\vec{H},\mathbf{v}\right)} \end{cases}, \tag{2}$$

where Q_{XX}, Q_{YY} and Q_{XY} are the second-order moments of the PSF,

$$\begin{cases} Q_{XX}\left(\vec{H}, v\right) = \frac{\int \mathbf{I}\left(\vec{H},v;x,y\right)\mathbf{w}(x,y)(x-\bar{x})^2 dxdy}{\int \mathbf{I}\left(\vec{H},v;x,y\right)\mathbf{w}(x,y)dxdy} \\ Q_{XY}\left(\vec{H}, v\right) = \frac{\int \mathbf{I}\left(\vec{H},v;x,y\right)\mathbf{w}(x,y)(x-\bar{x})(y-\bar{y})dxdy}{\int \mathbf{I}\left(\vec{H},v;x,y\right)\mathbf{w}(x,y)dxdy} \\ Q_{YY}\left(\vec{H}, v\right) = \frac{\int \mathbf{I}\left(\vec{H},v;x,y\right)\mathbf{w}(x,y)(y-\bar{y})^2 dxdy}{\int \mathbf{I}\left(\vec{H},v;x,y\right)\mathbf{w}(x,y)dxdy} \end{cases}, \tag{3}$$

where **I** represents the two-dimensional intensity distribution of the PSF at certain field position with certain misalignment parameters, x and y are coordinates in the PSF image, $\bar{x}$ and $\bar{y}$ represent the centroid position of the PSF image, and **w** is a matrix representing Gaussian weighting coefficient.

The intensity distribution of a PSF at certain field position with certain misalignment parameters can be expressed according to Fourier optics and nodal aberration theory, which can be expressed as [15]

$$\mathbf{I}\left(\vec{H}, v\right) = \left\{ FT^{-1}\{\mathbf{P}\exp\left[i\frac{2\pi}{\lambda}\left(\mathbf{W}\left(\vec{H}, \mathbf{v}\right)\right)\right]\right\}^2, \tag{4}$$

where i is an imaginary unit, FT^{-1} is the inverse Fourier transform, and **P** is a two-dimensional matrix representing the intensity distribution of the exit pupil surface (the element value of the matrix is 1 in the normalized aperture, and the rest are 0). $\mathbf{W}\left(\vec{H}, \mathbf{v}\right)$ represents the wavefront phase at field $\vec{H}$ with system misalignment parameters **v**. Importantly, based on the framework of nodal aberration theory, $\mathbf{W}\left(\vec{H}, \mathbf{v}\right)$ can be expressed as the sum of two parts,

$$\mathbf{W}\left(\vec{H}, v\right) = \mathbf{W}_0\left(\vec{H}\right) + \mathbf{W}_M\left(\vec{H}, \mathbf{v}\right), \tag{5}$$

where $\mathbf{W}_0\left(\vec{H}\right)$ represents the aberration field in the original state which is determined by the optical design and mirror figures (unaffected by misalignments), and $\mathbf{W}_M\left(\vec{H}, \mathbf{v}\right)$ represents the net aberration field induced by misalignments, which can be expressed as a linear function of **v** and $\vec{H}$. The specific expression of $\mathbf{W}_M\left(\vec{H}, \mathbf{v}\right)$ can be referred to [15].

3. Active Alignment for Optimal Ellipticity Performance

Using Equations (1)–(5), the relationships between the PSF ellipticity at arbitrary field position and the misalignment parameters are established. On this basis, we can set average ellipticity across the field of view as objection function

$$E(v) = \frac{\sum_{k=1}^{K}\sqrt{\left[e_1\left(\vec{H}_k, \mathbf{v}\right)\right]^2 + \left[e_2\left(\vec{H}_k, \mathbf{v}\right)\right]^2}}{K}, \tag{6}$$

where K represents the number of sampling points in the field of view, and the specific value of it depends on the computing power and the calculation accuracy of the average ellipticity (for example, K is 11*11 in this paper, etc.). Particle swarm optimization algorithm is used in this paper. Gradient-based optimization algorithms can easily be trapped in

a local minimum, for the searching direction of them mainly depends on the derivative information of the error metric. At the same time, the objective function in this paper does not have an advantage in taking derivatives. From this perspective, PSO algorithms are better, for they rely directly upon objective function values rather than derivative information [44]. We set the learning factors c1 = 1.6, c2 = 2.65. The value of w is constant, w = 0.5, T = 0.001. The population size is 40 and the maximum number of iterations is 800. Using the numerical optimization tool, the set of misalignment parameter ($\mathbf{v}_0$) corresponding to the minimum average ellipticity can be obtained:

$$\mathrm{E}(\mathbf{v}_0) = \min\{\mathrm{E}(\mathbf{v})\}. \tag{7}$$

We can then obtain the aberration field corresponding to optimal ellipticity performance.

Note that in the process presented above, all the misalignment parameters are considered. However, when correcting aberration on orbit, only part of the parameters can be selected as compensating DOFs due to constraints in space. For large-aperture off-axis TMA telescopes with freeform surface, secondary mirror (SM) and fine steering mirror (FSM) can be selected as the compensating DOFs based on aberration compensation characteristics. Then, the aberration field corresponding to the optimal ellipticity performance is taken as the correction goal; the DOFs of the SM and FSM are utilized to achieve this goal.

The diagram of the proposed approach is illustrated in Figure 1. This approach can be divided into the following two parts:

(1) In the first part, we obtain the aberration field corresponding to the optimal ellipticity performance through optimization. The mean ellipticity value of 11*11 field points is taken as the objective function and the misalignments of each mirror are taken as the variable. Meanwhile, the relationships between the PSF ellipticity at arbitrary field position and the misalignment parameters are established based on Fourier optics and nodal aberration theory.

(2) In the second part, SM and the FSM are selected as the adjustable degrees of freedom for the optimal correction of ellipticity, and the adjustment amount of SM and FSM is calculated (multi-field wavefront aberrations are needed in advance).

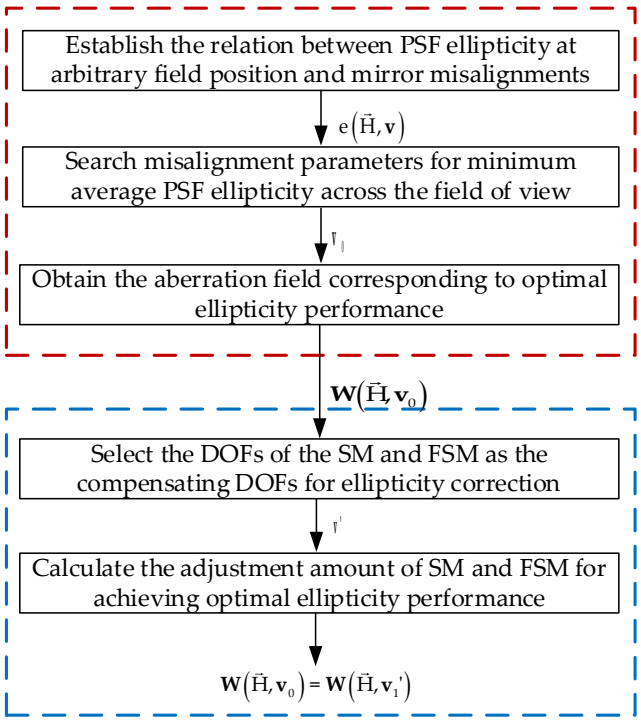

Figure 1. Diagram of the proposed on-orbit active alignment strategy for optimal ellipticity performance.

In Figure 1, $\mathbf{W}\left(\vec{\mathrm{H}}, \mathbf{v}_0\right)$ represents the aberration fields corresponding to the optimal ellipticity performance obtained in the first step using global optimization, $\mathbf{W}\left(\vec{\mathrm{H}}, \mathbf{v}_1'\right)$ represents the aberration fields after adjusting SM and FSM on orbit to achieve the optimal ellipticity performance.

4. Simulations

4.1. Optical System Used for Demonstrating the Proposed Active Alignment Strategy

In this paper, the optical system of the Chinese Space Station Telescope (CSST) is used to demonstrate the effectiveness of the proposed approach, which is a 2 m F/14 COOK-type unobscured off-axis three-mirror anastigmatic (TMA) telescope with 1.1° × 1° field of view (FOV). The optical layout of the CSST is shown in Figure 2, including primary mirror (PM), SM, tertiary mirror™, which is a freeform surface, a folding mirror (FM), which is used to correct image plane tilt and switch back-end astronomical measuring instruments, and an image plane (IMG) [45,46]. The materials used to manufacture mirrors of CSST are SiC [47–50].

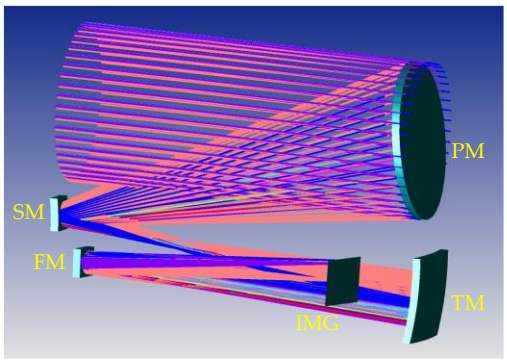

Figure 2. Optical layout of the CSST.

To maintain the exceptional image quality of the CSST, wavefront sensing and control (WFS and C) is vital to ensure the optical alignment of the telescope throughout the mission. For CSST, the five degrees of freedom (DOFs) of SM (XDE_{SM}, YDE_{SM}, ADE_{SM}, BDE_{SM} and ZDE_{SM}) and three DOFs of the FM (ADE_{FM}, BDE_{FM} and ZDE_{FM}) are selected as the adjustable DOFs to align and compensate for the effects of misalignments on wavefront aberrations (*XDE* and *YDE* are the mirror vertex decenters in the x-z and y-z plane, respectively, *BDE* and *ADE* are the mirror tip-tilts in the x-z and y-z plane, respectively, and *ZDE* represents the errors in spacing between mirrors). Specifically, SM is used to compensate for the non-rotationally symmetric aberrations of the PM and TM. FM is used to correct defocused aberration and inclination of the image plane.

To evaluate the ellipticity performance of the CSST, 41 × 41 PSFs are generated by the CODE V corresponding to 41 × 41 field points uniformly distributed in the FOV. The PSF is sampled on a 512 × 512 grid with an image sampling step of 0.4 micron [4] in this section. In addition, the root mean square wavefront errors (RMS WFE) of these 41 × 41 field points are used to evaluate the wavefront aberration of the CSST. The full-field distribution of ellipticity and RMS WFE distribution in nominal state are shown in Figures 3a and 3b, respectively. The maximum and mean values are 0.0843 and 0.0234, as shown in Figure 3a. The maximum and mean values are 0.0523λ and 0.0256λ, as shown in Figure 3b.

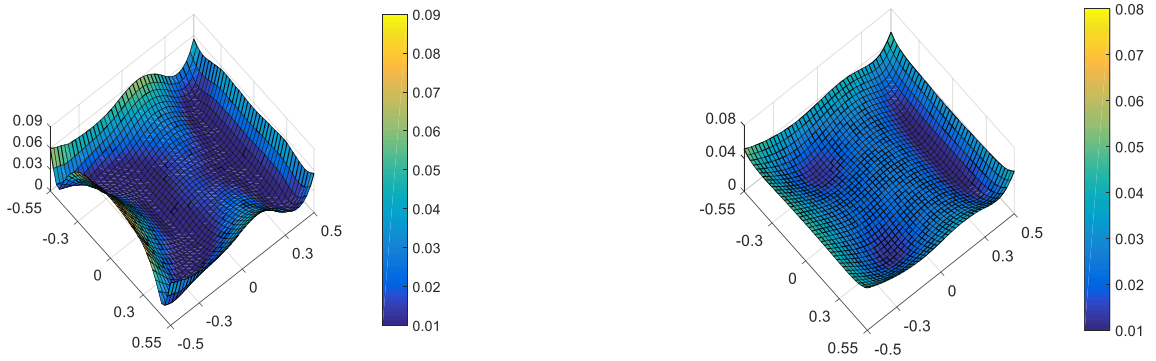

(**a**) (**b**)

Figure 3. Full-field distribution of ellipticity (**a**) and RMS WFE (**b**) in nominal state.

However, the mirror has certain surface deformations due to manufacturing error, gravity loading and other reasons. The existence of these deformations reduces the imaging quality of the system, which can also lead to changes in the ellipticity distribution of the system. According to the characteristics of the support structure of the CSST, the simulation group provides the surface deformation caused by changes in external environmental factors such as gravity unloading and temperature variations. These surface deformations can be loaded into the optical model through the CODE V software. The figures of each mirror (including surface deformation) considered in this paper are shown in Figure 4.

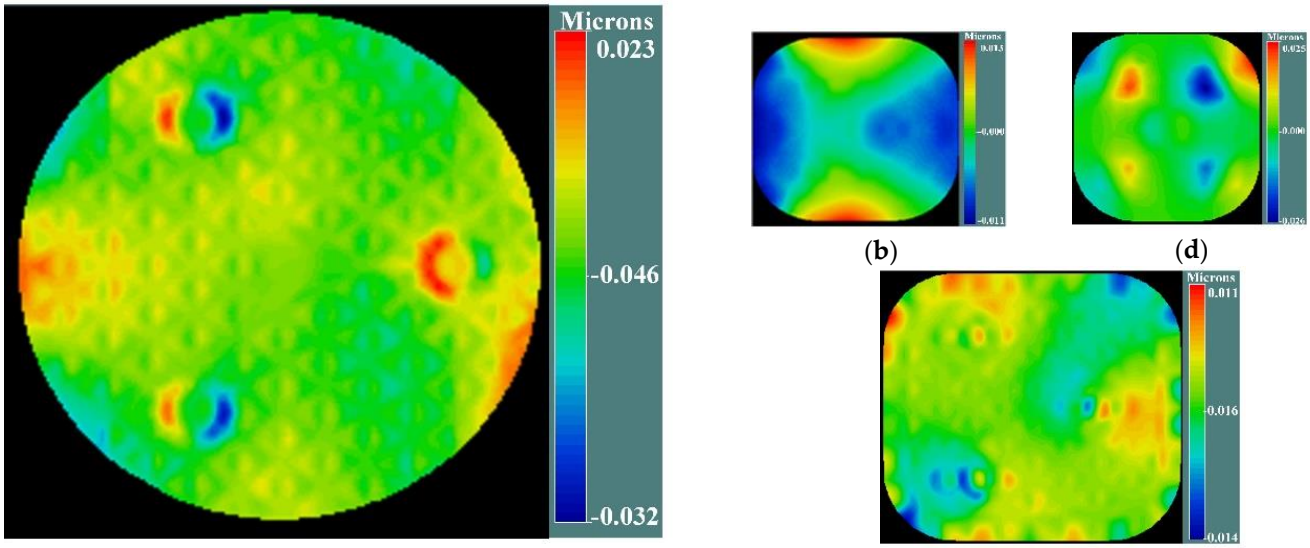

(**a**) (**b**) (**d**) (**c**)

Figure 4. The figure of each mirror (including surface deformation) considered in this paper for CSST: (**a**) figure of PM, (**b**) figure of SM, (**c**) figure of TM, (**d**) figure of FM.

The full-field distribution of ellipticity and the full-field distribution of RMS WFE distribution in the presence of surface deformation are shown in Figures 5a and 5b, respectively. The maximum and mean values are 0.1152 and 0.0351, as shown in Figure 5a. The maximum and mean values are 0.0778λ and 0.0472λ, as shown in Figure 5b. Comparing Figures 3 and 5, we can see that after introducing the set of surface deformations, both full-field distribution of ellipticity and RMS WFE deviate from the nominal state.

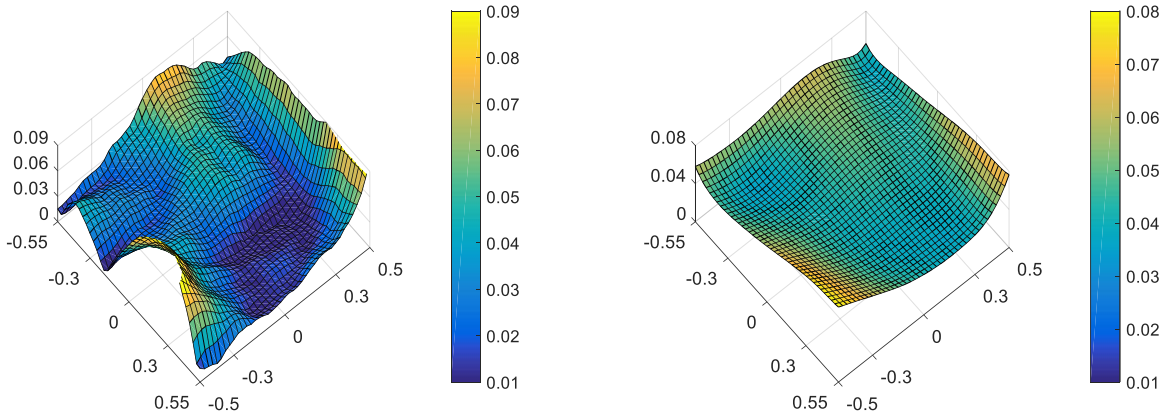

(**a**) (**b**)

Figure 5. Full-field distribution of ellipticity (**a**) and RMS WFE (**b**) in the presence of surface deformations.

4.2. Comparison of Ellipticity Distribution between the State of "Optimal Wavefront Aberration" and "Optimal Ellipticity Performance" in the Presence of Surface Deformation

The wavefront aberrations induced by surface deformations can be compensated by wavefront aberrations induced by misalignments to some extent (only the low-order wavefront aberrations induced by surface deformation can be compensated). In this section, full-field distribution of ellipticity and RMS WFE under different correction targets are compared in the presence of surface deformation.

On the one hand, "optimal wavefront aberration in the full FOV" is taken as the correction goal of on-orbit active optical alignment. Referring to JWST [5], the Sensitivity Table Method (STM) is selected to calculate the alignments of SM and FM for compensating wavefront aberrations. For the given set of surface deformations, the amount of adjustable DOFs required to correct the wavefront are $XDE_{SM} = -0.0367$ mm, $YDE_{SM} = 0.0061$ mm, $ZDE_{SM} = -0.0078$ mm, $ADE_{SM} = 0.0006°$, $BDE_{SM} = 0.0007°$, $ZDE_{FM} = 0.1178$ mm, $ADE_{FM} = 0.0019°$ and $BDE_{FM} = -0.0001°$. The full-field distribution of ellipticity and RMS WFE after correction are shown in Figures 6a and 6b, respectively. The maximum and mean values are 0.0857 and 0.0369 in Figure 6a. The maximum and mean values are 0.0647λ and 0.0426λ in Figure 6b.

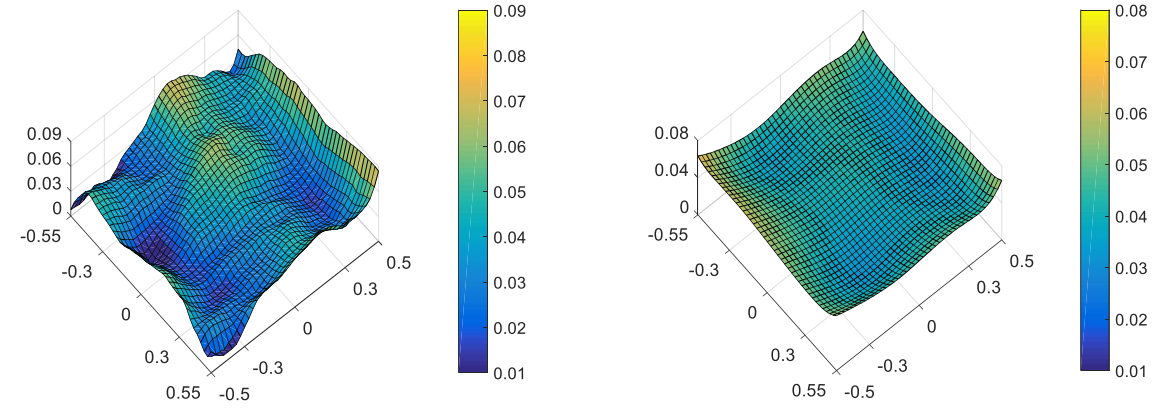

(**a**) (**b**)

Figure 6. Full-field distribution of ellipticity (**a**) and RMS WFE (**b**) for the state of "optimal wavefront aberration".

On the other hand, "optimal ellipticity performance in the full FOV" described in Section 3 is taken as the correction goal of on-orbit active optical alignment. The amount of adjustable DOFs required to correct the ellipticity are XDE_{SM} = −0.0662 mm, YDE_{SM} = −0.0346 mm, ZDE_{SM} = 0.0068 mm, ADE_{SM} = −0.0013°, BDE_{SM} = 0.0019°, ZDE_{FM} = −0.0040 mm, ADE_{FM} = 0.0003° and BDE_{FM} = −0.0029°. The full-field distribution of ellipticity and RMS WFE after correction are shown in Figure 7a,b. The maximum and mean values are 0.0670 and 0.0228, as shown in Figure 7a. The maximum and mean values of RMS WFE are 0.0825λ and 0.0492λ, as shown in Figure 7b.

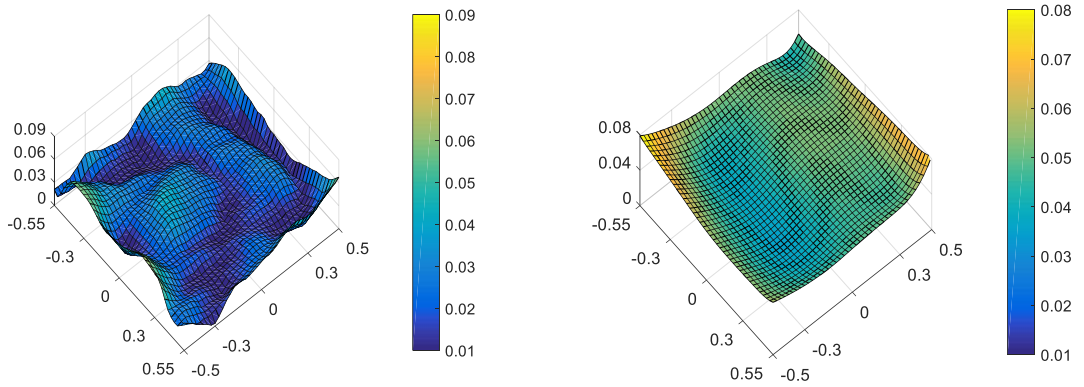

(**a**) (**b**)

Figure 7. Full-field distribution of ellipticity (**a**) and RMS WFE (**b**) for the state of "optimal ellipticity performance".

Comparing Figures 6 and 7, we can recognize that a different correction goal will lead to a different ellipticity and RMS WFE performance, as shown in Table 1. Importantly, the mean value of ellipticity in the full FOV for the state of "optimal wavefront aberration" and the state of "optimal ellipticity performance" are 0.0369 and 0.0228, respectively. This fact demonstrates that the method proposed in this paper can effectively improve the ellipticity performance. Meanwhile, the mean value of RMS WFE in the full FOV for the state of "optimal wavefront aberration" and the state of "optimal ellipticity performance" are 0.0426 and 0.0492, respectively. The mean value of RMS WFE in the full FOV for the state of "optimal ellipticity performance" is also acceptable (which is still within the diffraction limit).

Table 1. The typical values of ellipticity and RMS WFE in the different state.

Different State	Ellipticity		RMS WFE	
	Maximum Values	Mean Values	Maximum Values	Mean Values
Nominal state	0.0843	0.0234	0.0523λ	0.0256λ
In the presence of surface deformations	0.1152	0.0351	0.0778λ	0.0472λ
"Optimal wavefront aberration"	0.0857	0.0369	0.0647λ	0.0426λ
"Optimal ellipticity performance"	0.0670	0.0228	0.0825λ	0.0492λ

4.3. Comparison of Ellipticity Distribution between the State of "Optimal Wavefront Aberration" and "Optimal Ellipticity Performance" in the Presence of Surface Deformation and Mirror Misalignments

This subsection continues to discuss that the full-field distribution of ellipticity and RMS WFE under a different active alignment goal in the presence of both surface deformation and mirror misalignments (including lateral and axial misalignments [25–27]).

A set of random mirror misalignment is generated within the predicted misalignment ranges, which are presented below: XDE_{PM} = −0.0032 mm, YDE_{PM} = 0.0020 mm, ZDE_{PM} = 0.0036 mm, ADE_{PM} = 0.0002°, BDE_{PM} = 0.0009°, XDE_{SM} = 0.0033 mm, YDE_{SM} = −0.0001 mm, ZDE_{SM} = −0.0042 mm, ADE_{SM} = 0.0004°, BDE_{SM} = 0.0009°,

XDE_{TM} = 0.0031 mm, YDE_{TM} = −0.0041 mm, ZDE_{TM} = 0.0033 mm, ADE_{TM} = 0.0009°, BDE_{TM} = −0.0003°, XDE_{FM} = −0.0007 mm, YDE_{FM} = −0.0042 mm, ZDE_{FM} = −0.9935 mm, ADE_{FM} = 0.0008° and BDE_{FM} = 0.0001°. The full-field distribution of ellipticity and RMS WFE in the presence of both surface deformation and mirror misalignments are shown in Figures 8a and 8b, respectively. The maximum and mean values are 0.1641 and 0.0854, as shown in Figure 8a. The maximum and mean values are 0.6881λ and 0.6448λ, as shown in Figure 8b.

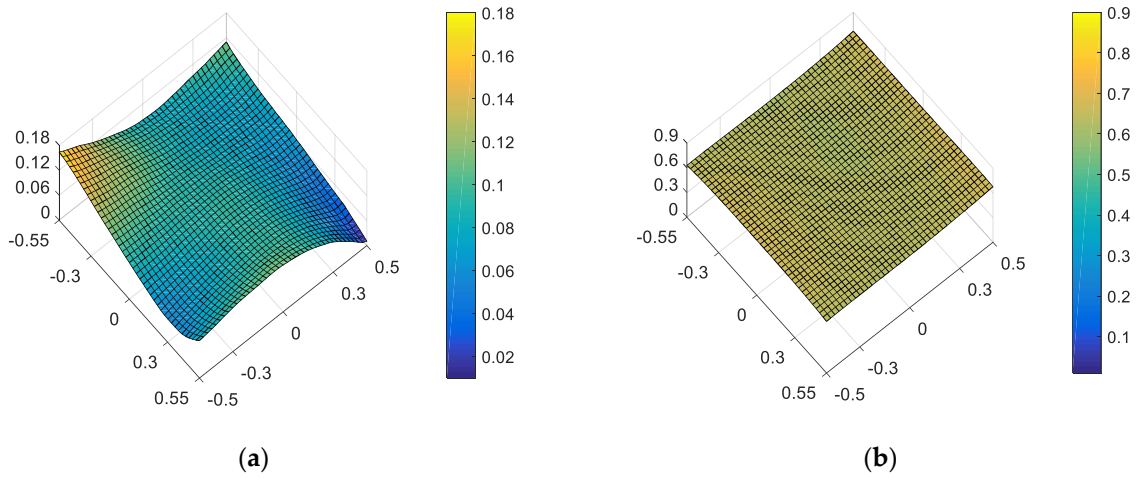

(**a**) (**b**)

Figure 8. Full-field distribution of ellipticity (**a**) and RMS WFE (**b**) in the presence of surface deformation and mirror misalignments.

Comparing Figures 5 and 8, it can be seen that the influence of mirror misalignments on the full-field distribution of ellipticity and RMS WFE is more obvious than the influence of surface deformation. Therefore, it is of great significance to verify the correction effect of a different correction goal on the full-field distribution of ellipticity and RMS WFE in the presence of both surface deformation and mirror misalignments.

On the one hand, "optimal wavefront aberration in the full FOV" is taken as the correction goal of on-orbit active optical alignment. For the given set of and surface deformation and mirror misalignments, the amounts of adjustable DOFs required to correct the wavefront are XDE_{SM} = 0.0497 mm, YDE_{SM} = 0.0069 mm, ZDE_{SM} = 0.0065 mm, ADE_{SM} = 0.0006°, BDE_{SM} = 0.0003°, ZDE_{FM} = 1.0107 mm, ADE_{FM} = −0.0011° and BDE_{FM} = 0.0028°. The full-field distribution of ellipticity and RMS WFE after correction are shown in Figures 9a and 9b, respectively. The maximum and mean values are 0.0810 and 0.0374, as shown in Figure 9a. The maximum and mean values are 0.0633λ and 0.0430λ, as shown in Figure 9b.

On the other hand, "optimal ellipticity performance in the full FOV" described in Section 3 is taken as the correction goal of on-orbit alignment. For the given set of surface deformation and mirror misalignments, the amounts of adjustable DOFs required to correct the ellipticity are XDE_{SM} = 0.0202 mm, YDE_{SM} = −0.0339 mm, ZDE_{SM} = 0.0213 mm, ADE_{SM} = −0.0013°, BDE_{SM} = 0.0015°, ZDE_{FM} = 0.8872 mm, ADE_{FM} = −0.0028° and BDE_{FM} = 0.0000°. The full-field distribution of ellipticity and RMS WFE after correction are shown in Figures 10a and 10b, respectively. The maximum and mean values are 0.0664 and 0.0233, as shown in Figure 10a. The maximum and mean values are 0.0807λ and 0.0486λ, as shown in Figure 10b.

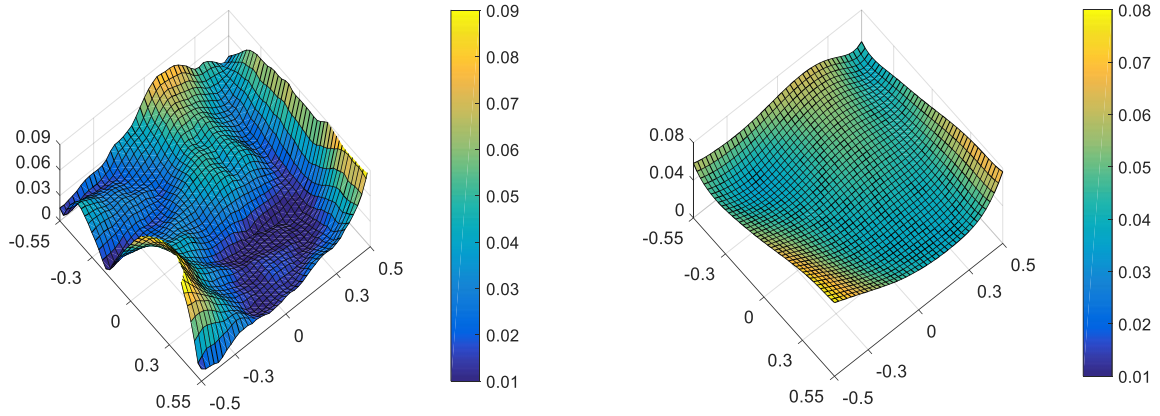

(**a**) (**b**)

Figure 9. Full-field distribution of ellipticity and RMS WFE after optimizing by optimal wavefront aberration: (**a**) ellipticity distribution and (**b**) RMS WFE distribution.

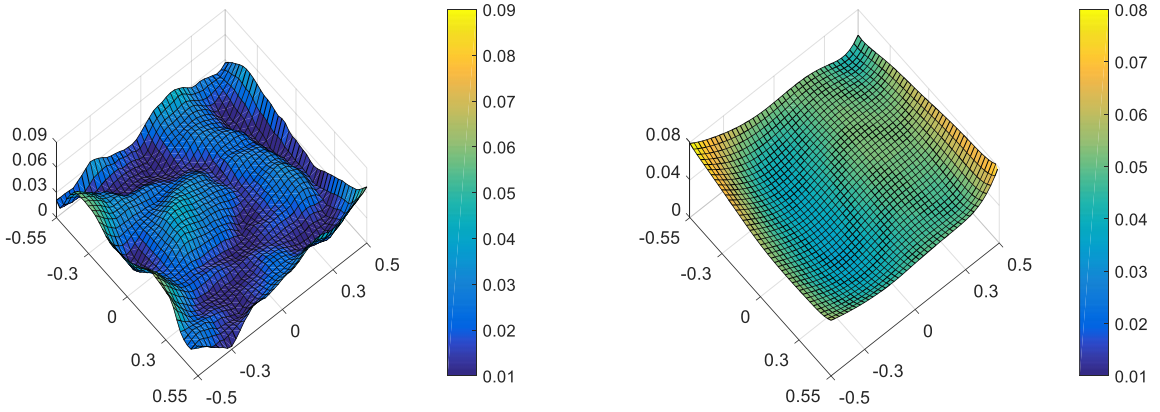

(**a**) (**b**)

Figure 10. Full-field distribution of ellipticity and RMS WFE after optimizing by optimal ellipticity performance: (**a**) ellipticity distribution and (**b**) RMS WFE distribution.

Comparing Figures 9 and 10, we can further conclude that a different correction goal leads to a different ellipticity performance and RMS WFE performance, as shown in Table 2. From Figures 7 and 10, it can be clearly seen that the method proposed by this paper has a certain correction effect on the ellipticity performance with the mean value of the RMS WFE under 1/14λ. On-orbit active alignment method with the goal of optimal ellipticity performance can effectively optimize the full-field ellipticity performance. While the RMS WFE in this state is not optimal, it is still comparable to the state of "optimal RMS WFE". Therefore, the proposed method is specifically suitable for the case where high ellipticity performance is required in the presence of both surface deformation and mirror misalignments.

Table 2. The typical values of ellipticity and RMS WFE in the different state for complex working condition.

Different State	Ellipticity		RMS WFE	
	Maximum Values	Mean Values	Maximum Values	Mean Values
Nominal state	0.0843	0.0234	0.0523λ	0.0256λ
In the presence of complex working condition	0.1641	0.0854	0.6881λ	0.6448λ
"Optimal wavefront aberration"	0.0810	0.0374	0.0633λ	0.0430λ
"Optimal ellipticity performance"	0.0664	0.0233	0.0807λ	0.0486λ

From Figures 6, 7, 9 and 10, it can be seen that mirror misalignments do not change the optimal full-field distribution of ellipticity and RMS WFE within a certain range of misalignments, which is consistent with the aberration compensation theory. Some valuable insights into aberration field characteristics about on-orbit active alignment are discussed in the next section.

5. Results

Some valuable insights into aberration field characteristics corresponding to optimal ellipticity performance are presented in this section. The full-field distribution of defocus, astigmatism and coma in a different state are shown in Figures 11–13.

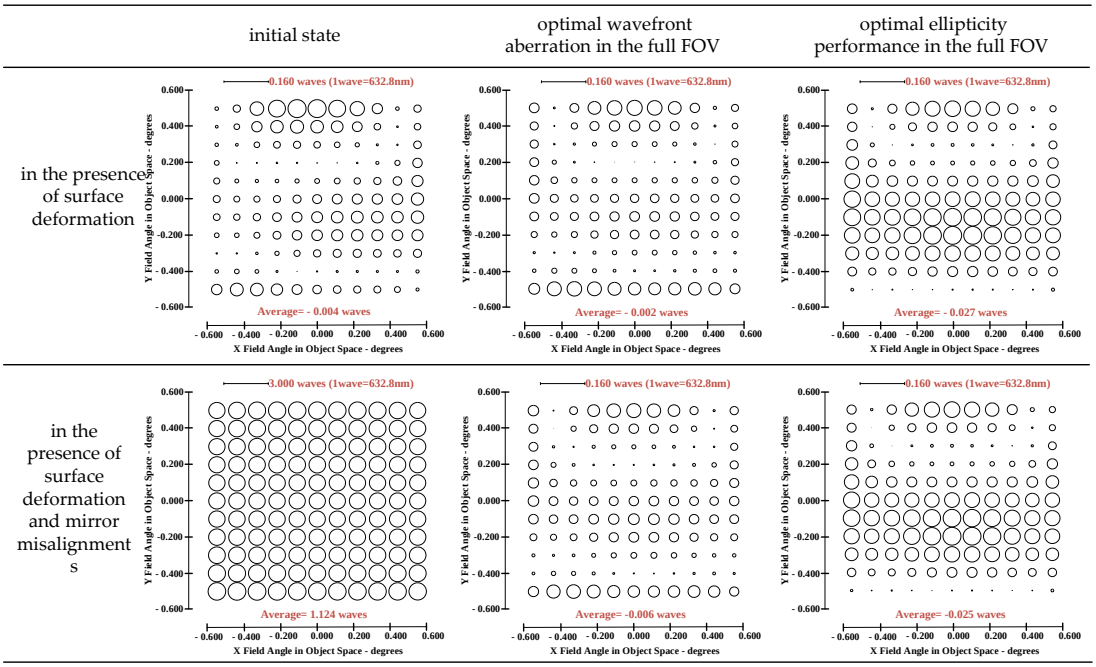

Figure 11. FFDs for defocus (Z4).

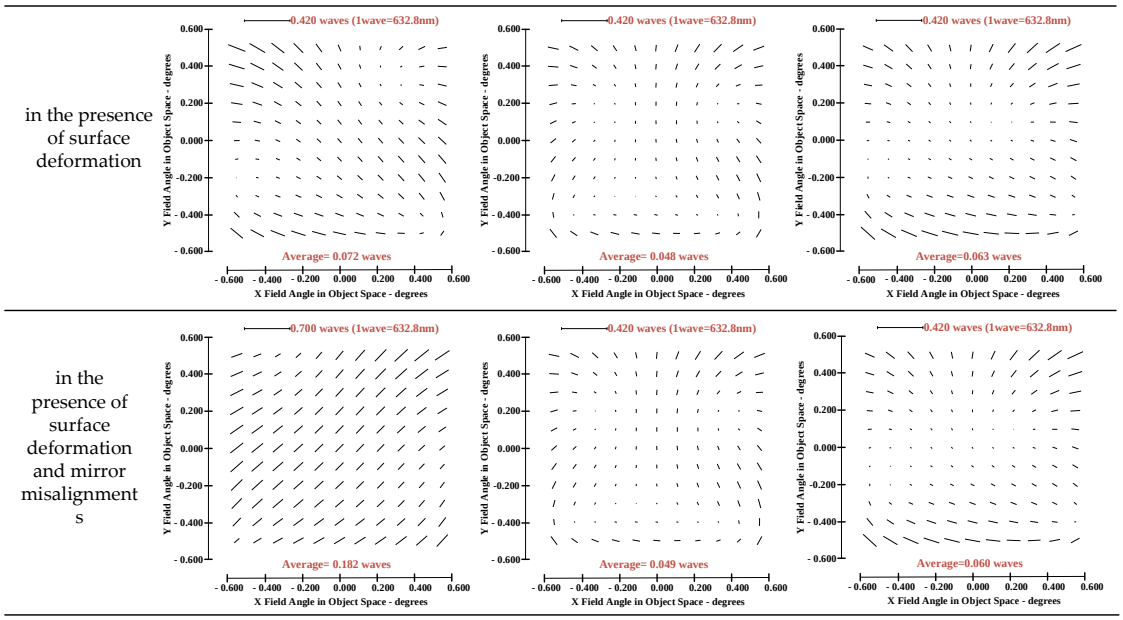

Figure 12. FFDs for astigmatism (Z5/Z6).

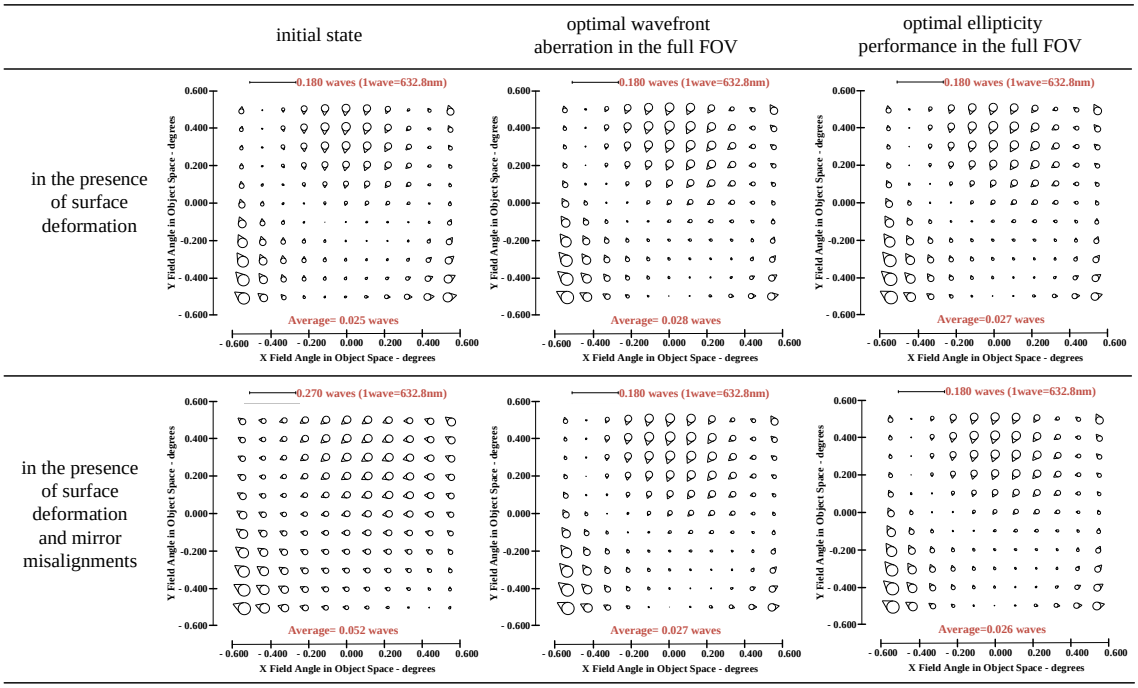

Figure 13. FFDs for coma (Z7/Z8).

The following conclusions can be drawn from Figures 11–13:

(1) The full-field distribution of defocus and astigmatism is the main factor affecting the full-field distribution of ellipticity, while the full-field distribution of coma has little influence on the full-field distribution of ellipticity.

(2) At the same field point, different values of defocus and astigmatism can produce different values of ellipticity. On orbit, the full-field distribution of ellipticity can be corrected by adjusting the full-field distribution of defocus and astigmatism.

(3) There exists an inherent relationship between the proportion of full-field distribution of defocus and astigmatism for the state of "optimal ellipticity performance": if the value of defocused aberration at a certain field point is comparatively large, the value of astigmatism at the corresponding point is relatively small, and if the value of astigmatism at certain field point is large, the value of defocus at the corresponding field point is relatively small. However, there is no similar "relationship" when the correction goal is "optimal wavefront error".

6. Conclusions

This paper proposes an active optical alignment strategy to achieve optimal ellipticity performance and demonstrates that there exists certain difference between the state of "optimal ellipticity performance" and the state of "optimal wavefront error". Based on the framework of nodal aberration theory (NAT), an active alignment method of large-aperture space telescopes for optimal ellipticity performance is proposed, where the aberration field distribution corresponding to the optimal full field-of-view ellipticity is determined with global optimization, and the degrees of freedom (DOFs) of the secondary mirror and the folded flat mirror are taken as the compensation DOFs to achieve the optimal ellipticity performance. The simulations show that the mean ellipticity value corresponding to optimal ellipticity performance is 0.03, while this value is 0.04 for optimal wavefront performance (the optical system of CSST is used for simulation). Some valuable insights into aberration field characteristics corresponding to the optimal ellipticity performance are presented, which shows that the proportion between astigmatic aberration field and medial focal surface can affect the ellipticity performance. In practice, we can change the goal of on-orbit alignment from "optimal wavefront error" to the goal of "optimal ellipticity

performance" if a higher ellipticity performance is required. This work lays a basis for the correction of ellipticity for complicated optical systems.

Author Contributions: X.B. and G.J. designed this research; X.B. and X.G. contributed to the theory research; X.B., B.X., F.J. and Z.L. performed the simulations; X.B. analyzed the data; X.B. and G.J. wrote the paper and created the diagrams; X.B. and S.X. contributed to scientific advising and proof-reading. All authors have read and agreed to the published version of the manuscript.

Funding: This research was funded by project of special research assistant of the Chinese Academy of Sciences and National Natural Science Foundation of China (NSFC) (62205334, 61905241). I am sorry to say that there is no Fund code for project of special research assistant of the Chinese Academy and just keep this sentence.

Institutional Review Board Statement: Not applicable.

Informed Consent Statement: Not applicable.

Data Availability Statement: Not applicable.

Acknowledgments: The authors thank Synopsys for providing the research license of CODE V.

Conflicts of Interest: The authors declare no conflict of interest.

References

1. Bartelmann, M.; Schneider, P. Weak gravitational lensing. *Phys. Rep.* **2001**, *340*, 291–472. [CrossRef]
2. The Shear Testing Programme—I. Weak lensing analysis of simulated ground-based observations. *Mon. Not. R. Astron. Soc.* **2006**, *368*, 1323–1339. [CrossRef]
3. Paulin-Henriksson, S.; Amara, A.; Voigt, L.; Refregier, A.; Bridle, S.L. Point spread function calibration requirements for dark energy from cosmic shear. *Astron. Astrophys.* **2008**, *484*, 67–77. [CrossRef]
4. Zeng, F.; Zhang, X.; Zhang, J.; Shi, G.; Wu, H. Optics ellipticity performance of an unobscured off-axis space telescope. *Opt. Express* **2014**, *22*, 25277–25285. [CrossRef]
5. Howard, J.M.; Angeli, G.Z.; Cullum, M.J.; Ha, K.Q.; Shiri, R.; Smith, J.S.; Mosier, G.; Muheim, D. Optical modeling activities for NASA's James Webb Space Telescope (JWST): Part V. Operational alignment updates. In *Modeling, Systems Engineering, and Project Management for Astronomy III*; SPIE: Bellingham, WA, USA, 2008; pp. 295–304.
6. Wilson, R.N.; Franza, F.; Noethe, L. Active optics. I. A system for optimizing the optical quality and reducing the costs of large telescopes. *J. Mod. Opt.* **1987**, *34*, 485–509. [CrossRef]
7. Kim, E.D.; Choi, Y.W.; Kang, M.S.; Choi, S.C. Reverse-optimization Alignment Algorithm using Zernike Sensitivity. *J. Opt. Soc. Korea* **2005**, *9*, 68–73. [CrossRef]
8. Liu, Z.; Qi, P.; Xu, Y.; Ma, H.; Ren, G. Misalignment calculation on off-axis telescope system via fully connected neural network. *IEEE Photonics J.* **2020**, *12*, 1–12. [CrossRef]
9. Lundgren; Mark, A. Alignment of a three-mirror off-axis telescope by reverse optimization. *Opt. Eng.* **1991**, *30*, 307–311. [CrossRef]
10. Dominguez, M.Z.; Kang, H.; Kim, S.; Berrier, J.; Kim, D.W. Multi-field merit-function-based regression method for Wide Field Infrared Survey Telescope grism system alignment. *Appl. Opt.* **2019**, *58*, 6802. [CrossRef]
11. Kim, S.; Yang, H.S.; Lee, Y.W.; Kim, S.W. Merit function regression method for efficient alignment control of two-mirror optical systems. *Opt. Express* **2007**, *15*, 5059–5068. [CrossRef]
12. Lee, H.; Dalton, G.; Tosh, I.; Kim, S. Computer-guided alignment I: Phase and amplitude modulation of alignment-influenced optical wavefront. *Opt. Express* **2007**, *15*, 3127–3139. [CrossRef] [PubMed]
13. Lee, H.; Dalton, G.B.; Tosh, I.A.J.; Kim, S.W. Computer-guided alignment II:Optical system alignment using differential wavefront sampling. *Opt. Express* **2007**, *15*, 15424–15437. [CrossRef] [PubMed]
14. Lee, H.; Dalton, G.B.; Tosh, I.A.J.; Kim, S.W. Computer-guided alignment III: Description of inter-element alignment effect in circular-pupil optical systems. *Opt. Express* **2008**, *16*, 10992. [CrossRef]
15. Guohao, J.U.; Ma, H.; Xu, B.; Wang, S.; Xu, S. Active alignment of space astronomical telescopes by matching arbitrary multi-field stellar image features. *Opt. Express* **2021**, *29*, 24446–24465.
16. Zhengyang, L.B.Y.X.L. Active Alignment Method of Telescope Based on Star Ellipticity of MultiFieldofView. *Acta Photonica Sin.* **2021**, *50*, 0412002.
17. Wu, W.; Luo, Z.; Yang, H.; Cao, Y.; Shang, J. Misalignments calculation method for optical systems based on the ellipticity distribution of stellar image. *Infrared Laser Eng.* **2022**, *51*, 20210391.
18. Thompson, K.P. *Aberration Fields in Tilted and Decentered Optical Systems*; The University of Arizona: Tucson, AZ, USA, 1980.
19. Thompson, K.P. Description of the third-order optical aberrations of near-circular pupil optical systems without symmetry. *J. Opt. Soc. Am. A Opt. Image Sci. Vis.* **2005**, *22*, 1389–1401. [CrossRef]

20. Thompson, K.P. Multinodal fifth-order optical aberrations of optical systems without rotational symmetry: Spherical aberration. *J. Opt. Soc. Am. A Opt. Image Sci. Vis.* **2009**, *26*, 1090–1100. [CrossRef]
21. Thompson, K.P. Multinodal fifth-order optical aberrations of optical systems without rotational symmetry: The comatic aberrations. *J. Opt. Soc. Am. A* **2010**, *27*, 1490–1504. [CrossRef]
22. Thompson, K.P. Multinodal fifth-order optical aberrations of optical systems without rotational symmetry: The astigmatic aberrations. *J. Opt. Soc. America. A Opt. Image Sci. Vis.* **2011**, *28*, 821–836. [CrossRef]
23. Schmid, T. Misalignment Induced Nodal Aberration Fields and Their Use in Thealignment of Astronomical Telescopes. Ph.D. Thesis, University of Central Florida, Orlando, FL, USA, 2010.
24. Gu, Z.; Yan, C.; Wang, Y. Alignment of a three-mirror anastigmatic telescope using nodal aberration theory. *Opt. Express* **2015**, *23*, 25182. [CrossRef]
25. Ju, G.; Yan, C.; Gu, Z.; Ma, H. Aberration fields of off-axis two-mirror astronomical telescopes induced by lateral misalignments. *Opt. Express* **2016**, *24*, 24665–24703. [CrossRef] [PubMed]
26. Ju, G.; Ma, H.; Yan, C. Aberration fields of off-axis astronomical telescopes induced by rotational misalignments. *Opt. Express* **2018**, *26*, 24816. [CrossRef] [PubMed]
27. Guohao, J.; Changxiang, Y.; Zhiyuan, G.; Hongcai, M. Nonrotationally symmetric aberrations of off-axis two-mirror astronomical telescopes induced by axial misalignments. *Appl. Opt.* **2018**, *57*, 1399.
28. Xiaobin, Z.; Dong, Z.; Shuyan, X.; Hongcai, M. Active optical alignment of off-axis telescopes based on nodal aberration theory. *Opt. Express* **2016**, *24*, 26392.
29. Zhang, X.; Xu, S.; Ma, H.; Liu, N. Optical compensation for the perturbed three mirror anastigmatic telescope based on nodal aberration theory. *Opt. Express* **2017**, *25*, 12867–12883. [CrossRef]
30. Bai, X.; Ju, G.; Ma, H.; Xu, S. Aberrational interactions between axial and lateral misalignments in pupil-offset off-axis two-mirror astronomical telescopes. *Appl. Opt.* **2019**, *58*, 7693–7707. [CrossRef]
31. Schiesser, E.M.; Bauer, A.; Rolland, J.P. Estimating field-dependent nodal aberration theory coefficients from Zernike full-field displays by utilizing eighth-order astigmatism. *J. Opt. Soc. Am. A* **2019**, *36*, 2115. [CrossRef]
32. Bai, X.; Xu, B.; Ma, H.; Gao, Y.; Ju, G. Aberration fields of pupil-offset off-axis two-mirror astronomical telescopes induced by ROC error. *Opt. Express* **2020**, *28*, 30447. [CrossRef]
33. Bai, X.; Xu, B.; Ju, G.; Ma, H.; Zhang, C.; Wang, S.; Xu, S. Aberration compensation strategy for the radius of curvature error of the primary mirror in off-axis three-mirror anastigmatic telescopes. *Appl. Opt.* **2021**, *60*, 6199–6212. [CrossRef]
34. Karcı, Ö.; Arpa, E.; Ekinci, M.; Rolland, J.P. Experimental investigation of binodal astigmatism in nodal aberration theory (NAT) with a Cassegrain telescope system. *Opt. Express* **2021**, *29*, 19427–19440. [CrossRef] [PubMed]
35. Karcı, Ö.; Yeiltepe, M.; Arpa, E.; Wu, Y.; Ekinci, M.; Rolland, J.P. Experimental investigation in nodal aberration theory (NAT): Separation of astigmatic figure error from misalignments in a Cassegrain telescope. *Opt. Express* **2022**, *30*, 11150–11164. [CrossRef] [PubMed]
36. Zhao, N.; Papa, J.C.; Fuerschbach, K.; Qiao, Y.; Rolland, J.P. Experimental investigation in nodal aberration theory (NAT) with a customized Ritchey-Chrétien system: Third-order coma. *Opt. Express* **2018**, *26*, 8729–8743. [CrossRef] [PubMed]
37. He, X.; Luo, J.; Wang, J.; Zhang, X.; Liu, Y. Improvement of a computer-aided alignment algorithm for the nonsymmetric off-axis reflective telescope. *Appl. Opt.* **2021**, *60*, 2127–2140. [CrossRef] [PubMed]
38. Bernstein, G.M.; Jarvis, M. Shapes and Shears, Stars and Smears: Optimal Measurements for Weak Lensing. *Astron. J.* **2002**, *123*, 583–618. [CrossRef]
39. Kuijken, K. Shears from shapelets. *Astron. Astrophys.* **2006**, *456*, 827–838. [CrossRef]
40. Erben, T.; Van, W.L.; Bertin, E.; Mellier, Y.; Schneider, P. How accurately can we measure weak gravitational shear? *Astron. Astrophys.* **2000**, *366*, 717–735. [CrossRef]
41. Laureijs, R.; Amiaux, J.; Arduini, S.; Augueres, J.-L.; Zucca, E. *Euclid Definition Study Report*; HAL-OBSPM: Paris, France, 2011.
42. John, E.; Richard, N.; Felix, S.B. 20 years of Hubble Space Telescope optical modeling using Tiny Tim. *Proc. SPIE-Int. Soc. Opt. Eng.* **2012**, *8127*, 777–785.
43. Krist, J.; Hook, R. *The TinyTim User's Guide*; Baltimore Stsci: Baltimore, MD, USA, 2004.
44. Xin, Q.; Guohao, J.; Shuyan, X. Efficient solution to the stagnation problem of the particle swarm optimization algorithm for phase diversity. *Appl. Opt.* **2018**, *57*, 2747–2757.
45. Gong, Y.; Liu, X.; Cao, Y.; Chen, X.; Fan, Z.; Li, R.; Li, X.D.; Li, Z.; Zhang, X.; Zhan, H. Cosmology from the Chinese Space Station Optical Survey (CSS-OS). *Astrophys. J.* **2019**, *883*, 203. [CrossRef]
46. Luo, J.; He, X.U.; Fan, K.; Zhang, X. Effects of polarization aberrations in an unobscured off-axis space telescope on its PSF ellipticity. *Opt. Express* **2020**, *28*, 37958–37970. [CrossRef] [PubMed]
47. Wang, K.; Dong, J. Structural design of Φ2 m-level large-diameter SiC reflector used in space remote sensor. *Infrared Laser Eng.* **2017**, *46*, 718005. [CrossRef]
48. Wang, K.; Dong, J.; Wang, X.; Chi, C. Design of frame-type support structure for space-based rectangular convex mirror tested on the back. *Opt.-Int. J. Light Electron Opt.* **2020**, *212*, 164673.

49. Wang, K.; Dong, J.; Zhao, Y.; Chi, C.; Jiang, P.; Wang, X. Research on high performance support technology of space-based large aperture mirror. *Opt. Z. Fur Licht-Und Elektron. J. Light-Electronoptic* **2021**, *226*, 165929. [CrossRef]
50. Zhang, X.; Hu, H.; Wang, X.; Luo, X.; Zhang, G.; Zhao, W.; Wang, X.; Liu, Z.; Xiong, L.; Qi, E. Challenges and strategies in high-accuracy manufacturing of the world's largest SiC aspheric mirror. *Light Sci. Appl.* **2022**, *11*, 13. [CrossRef]